Enhancing Structural Reliability Analysis with Machine Learning-Based Surrogate Models: Theoretical and Experimental Insights

Alexandre Saidi, Lun Shao, Abdelmalek Zine, Mohamed Ichchou

▶ **To cite this version:**

Alexandre Saidi, Lun Shao, Abdelmalek Zine, Mohamed Ichchou. Enhancing Structural Reliability Analysis with Machine Learning-Based Surrogate Models: Theoretical and Experimental Insights. 2025. ⟨hal-05146445⟩

HAL Id: hal-05146445

https://hal.science/hal-05146445v1

Preprint submitted on 5 Jul 2025

HAL is a multi-disciplinary open access archive for the deposit and dissemination of scientific research documents, whether they are published or not. The documents may come from teaching and research institutions in France or abroad, or from public or private research centers.

L'archive ouverte pluridisciplinaire **HAL**, est destinée au dépôt et à la diffusion de documents scientifiques de niveau recherche, publiés ou non, émanant des établissements d'enseignement et de recherche français ou étrangers, des laboratoires publics ou privés.

HAL Authorization

Enhancing Structural Reliability Analysis with Machine Learning-Based Surrogate Models: Theoretical and Experimental Insights

Lun SHAO[a], Alexandre SAIDI[b], Abdel-Malek ZINE[c], Mohamed ICHCHOU[a]

[a] *Laboratory of Tribology and Dynamics of Systems, Ecole Centrale Lyon, Ecully, France*
[b] *Computer Science Laboratory for Image Processing and Information Systems, Ecole Centrale Lyon, Ecully, France*
[c] *Institut Camille Jordan, Ecole Centrale Lyon, Ecully, France*

Abstract

This paper presents a comprehensive framework for structural dynamics and reliability analysis by integrating theoretical modeling of continuous systems and experimental investigations of multi-storey steel frames. First, a beam-like structure with infinite degrees of freedom is analyzed using the Rayleigh-Ritz method, highlighting the importance of partial differential equations in capturing distributed mass, stiffness, and damping. Tuned Mass Dampers (TMDs) are incorporated to mitigate resonant vibrations, and advanced sampling techniques (Latin Hypercube Sampling, Monte Carlo simulation) are employed to quantify structural reliability under uncertain loading conditions. Machine learning models, including Random Forest and Neural Networks, are then developed as surrogate models to predict failure probabilities, revealing critical nonlinear relationships between system parameters. To validate and extend these insights, the framework is applied to a two-storey steel frame tested under controlled laboratory conditions. A mechanical shaker supplies dynamic excitations with varying statistical characteristics—kurtosis, root mean square (RMS), skewness, and crest factor—while force and acceleration measurements capture the structure's real-time responses. By training machine learning algorithms (Random Forest, Gradient Boosting, XGBoost, and Neural Networks) on time-domain features, the study demonstrates the capability of data-driven methods to capture complex vibratory behaviors beyond what standard mechanical models predict. The results offer important guidance for integrating advanced computational

tools, experimental data, and machine learning to enhance the structural reliability assessment of beam-like and frame structures alike.

Keywords: Continuous systems, Rayleigh-Ritz method, Tuned Mass Dampers, Reliability analysis, Surrogate modeling, Vibration control

---

1. Introduction

Modern engineering structures—such as tall buildings [1], long-span bridges, industrial machinery, and aerospace components—are becoming increasingly complex and are subjected to diverse, often stochastic loading conditions. Ensuring these systems maintain their structural integrity and reliability throughout their intended service life is paramount. Traditionally, Structural Reliability Analysis (SRA) has relied on deterministic or semi-probabilistic methods based on simplified assumptions [2, 3]. While these foundational approaches are valuable, they often struggle to address the inherent complexities of real-world systems, where multiple sources of uncertainty—such as material properties, geometric variabilities, environmental forces, and operational scenarios—interact in nonlinear ways [4, 5].

To mitigate the adverse effects of dynamic forces from wind, seismic events, and other external excitations, Tuned Mass Dampers (TMDs) [6, 7, 8, 9] are widely adopted. Traditional studies typically focus on simpler configurations, such as single-degree-of-freedom (1-DOF) or two-degree-of-freedom (2-DOF) models, providing fundamental insights into vibration reduction. However, real-world structures often involve multiple degrees of freedom (MDOF), introducing significant modeling and computational challenges when assessing their reliability. In scenarios with uncertainties in parameters and external loads, Monte Carlo Simulation (MCS) has proven to be a robust technique for evaluating structural reliability, particularly for random vibration problems [10, 11]. Nevertheless, the high computational cost of extensive simulations becomes impractical as the number of degrees of freedom—and consequently the system's complexity—increases.

Recent research [12, 13, 14, 15, 16] has explored hybrid strategies that integrate simulation-based methods with machine learning (ML) to alleviate this computational burden [17, 18]. In these hybrid approaches, ML models serve as surrogate predictors for system responses, significantly reducing the number of required high-fidelity simulations. These ML surrogates enable near-real-time reliability assessments, informed decision-making, and proac-

tive maintenance strategies. Thus, the convergence of probabilistic modeling, advanced simulation techniques, and ML-based surrogates presents a promising approach to addressing both industrial and scientific challenges in structural engineering.

However, traditional single-degree-of-freedom (and multi-degree-of-freedom (MDOF)) formulations, while foundational, fall short when dealing with distributed mass and continuous deformation profiles. To address these limitations, this work focuses on continuous beam-like structures governed by partial differential equations rather than ordinary differential equations. By employing the Rayleigh-Ritz method, we approximate the behavior of longitudinal and transverse vibrations in beams and evaluate the effectiveness of Tuned Mass Dampers in mitigating resonance effects.

Theoretical and numerical models alone do not guarantee accurate predictions, especially under uncertainties in loading conditions, material properties, and boundary constraints. Therefore, reliability analysis methods such as Latin Hypercube Sampling and Monte Carlo simulation are introduced [19, 20, 21], providing probabilistic estimates of failure. Furthermore, machine learning models—particularly ensemble methods like Random Forest and Gradient Boosting, as well as Neural Networks—are proposed as surrogate models to expedite reliability predictions and capture complex parameter interactions.

To validate the theoretical and numerical findings, the second part of this paper describes an experimental program conducted on a two-storey steel frame. A mechanical shaker imparts a range of dynamic excitations, characterized by time-domain features such as kurtosis, RMS, skewness, and crest factor. These features serve as inputs for a suite of machine learning algorithms, enabling a data-driven exploration of structural reliability under realistic laboratory conditions. By comparing predictions from various algorithms and analyzing feature importance, the study aims to identify the most effective statistical descriptors and modeling strategies for dynamic reliability assessments.

Ultimately, this integration of advanced theoretical modeling, probabilistic analysis, and experimental validation underscores the necessity of combining multiple techniques to gain a holistic understanding of structural behavior. The overarching goal is to enhance structural health monitoring, enable early damage detection, and support informed decision-making regarding maintenance and safety measures.

2. Longitudinal Vibration of a Beam with a TMD

The inclusion of a Tuned Mass Damper (TMD) is an effective strategy for mitigating vibrational responses in beam-like structures. In this work, we focus on longitudinal vibrations, which are typically simpler to analyze due to their one-dimensional nature. Although beams can also exhibit torsional and lateral vibrations—potentially coupled depending on cross-sectional asymmetry or pretwisting—the present study isolates the longitudinal response to highlight the influence of the TMD.

Figure 1 provides a schematic of the beam under consideration. One end of the beam is fixed, while the other end is equipped with a TMD composed of a mass, m_t, and a stiffness element, k_t. An external force $f(x,t)$ is applied along the beam's longitudinal axis x. The primary role of the TMD is to introduce a counteracting force at the free end, thereby reducing the overall vibration amplitude.

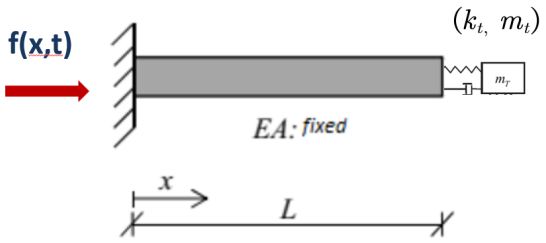

Figure 1: Schematic representation of the longitudinal vibration of a beam with a Tuned Mass Damper (TMD). The beam is fixed at one end, and the TMD is attached at the free end where it mitigates the dynamic response to the applied force $f(x,t)$.

The governing equation for the longitudinal displacement $u(x,t)$ is given by

$$EA\frac{\partial^2 u(x,t)}{\partial x^2} = \rho A\frac{\partial^2 u(x,t)}{\partial t^2} - f(x,t), \tag{1}$$

where E is the Young's modulus, A is the cross-sectional area, and ρ is the material density. The TMD imposes additional boundary conditions at the free end through its stiffness and mass, effectively coupling its motion with that of the beam.

A standard approach to solving this problem is via modal analysis. By expanding the beam displacement in terms of its mode shapes and corresponding time-dependent modal coordinates, one can incorporate the TMD's

effect on the boundary conditions. When tuned to one of the beam's resonant frequencies, the TMD's mass and stiffness (m_t and k_t) effectively absorb and dissipate vibratory energy, thereby reducing the amplitude of resonance peaks. This behavior provides improved dynamic performance and enhances the structural stability of the beam, demonstrating the potential of TMDs for controlling longitudinal vibrations.

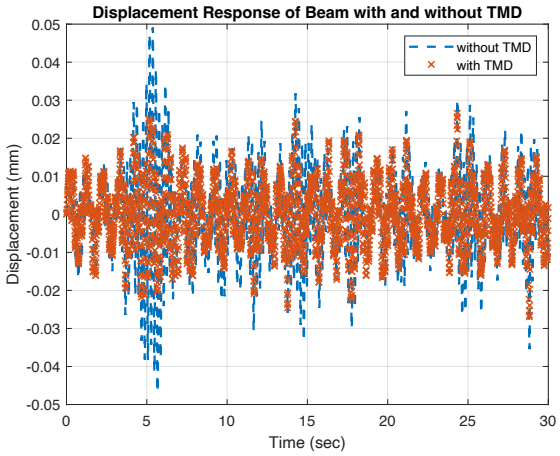

Figure 2: Comparison of the beam's longitudinal response with and without the TMD. The TMD reduces the peak displacement by providing a counteracting force at the free end, thereby mitigating vibrational amplitudes.

Fig. 2 illustrates a direct comparison of the beam's response with and without the TMD. A clear reduction in peak displacement can be observed, underscoring the effectiveness of the TMD in mitigating longitudinal vibrations.

2.1. Dynamic Analysis of Longitudinal Vibrations in a Beam with a TMD

To characterize the longitudinal dynamic behavior of the beam equipped with a TMD, the following analytical formulation is presented.

In the x direction, the displacement field for each frequency can be approximated by

$$\mu(x,t) = \sum_{i=1}^{n} \lambda_i(t)\, \psi_i(x), \tag{2}$$

where

- $i = 1, 2, \ldots, n$ indexes the number of terms in the approximation,
- $\lambda_i(t)$ is the Ritz coefficient, capturing the time-dependent component of the mode shape,
- $\psi_i(x)$ is the trial function, representing the spatial component of the mode shape.

At the fixed end ($x = 0$), the displacement satisfies the boundary condition

$$\mu(0, t) = 0. \tag{3}$$

This implies that the beam's displacement at the fixed support must remain zero at all times.

At the free end ($x = L$), the boundary condition is given by

$$EA\frac{\partial \mu(L,t)}{\partial x} = -k\,\mu(L,t) - c\,\frac{\partial \mu(L,t)}{\partial t} - m\,\frac{\partial^2 \mu(L,t)}{\partial t^2}, \tag{4}$$

where

- E is the Young's modulus of the beam material,
- A is the cross-sectional area of the beam,
- k, c, and m are the stiffness, damping, and mass of the TMD, respectively.

This boundary condition balances the internal axial force in the beam with the reactive forces introduced by the TMD, thereby governing the system's dynamic response at the free end.

2.1.1. Strain Energy of the System

The total strain energy of the system is given by

$$\begin{aligned} V &= V_{\text{beam}} + V_{\text{spring}} \\ &= \frac{1}{2}\int_0^L EA\left(\frac{\partial \mu}{\partial x}\right)^2 dx + \frac{1}{2}k_t\,\mu^2(x,t)\Big|_{x=L} \\ &= \frac{1}{2}\int_0^L EA\left(\sum_{i=1}^{n}\lambda_i\,\psi_i'(x)\right)^2 dx + \frac{1}{2}k_t\left(\sum_{i=1}^{n}\lambda_i\,\psi_i(L)\right)^2. \end{aligned}$$

Expanding further, we have

$$V = \frac{1}{2}\Big[\lambda_1\ \lambda_2\ \cdots\ \lambda_n\Big] \int_0^L EA\,\psi_i'(x)\,\psi_j'(x)\,dx \begin{bmatrix}\lambda_1\\ \lambda_2\\ \vdots\\ \lambda_n\end{bmatrix} + \Big[\lambda_1\ \lambda_2\ \cdots\ \lambda_n\Big] k_t\,\psi_i(L)\,\psi_j(L) \begin{bmatrix}\lambda_1\\ \lambda_2\\ \vdots\\ \lambda_n\end{bmatrix}.$$

The strain energy can then be written compactly in matrix form as

$$V = \frac{1}{2}\,\vec{\lambda}^T[K]\,\vec{\lambda}, \tag{5}$$

where $[K]$ is the stiffness matrix of the system, defined by

$$K_{ij} = \int_0^L EA\,\psi_i'(x)\,\psi_j'(x)\,dx + k_t\,\psi_i(L)\,\psi_j(L). \tag{6}$$

2.1.2. Kinetic Energy of the System

The total kinetic energy of the system is given by

$$\begin{aligned} T &= T_{\text{beam}} + T_{\text{mass}} \\ &= \frac{1}{2}\int_0^L \rho A \left(\frac{\partial \mu}{\partial t}\right)^2 dx + \frac{1}{2} m_t \left(\frac{\partial \mu}{\partial t}(L,t)\right)^2. \end{aligned}$$

After substituting the series expansion, we obtain

$$T = \frac{1}{2}\int_0^L \rho A \left(\sum_{i=1}^n \lambda_i\,\psi_i(x)\right)^2 dx + \frac{1}{2} m_t \left(\sum_{i=1}^n \lambda_i\,\psi_i(L)\right)^2.$$

Expanding further, we have

$$T = \frac{1}{2}\begin{bmatrix}\lambda_1 & \lambda_2 & \cdots & \lambda_n\end{bmatrix} \int_0^L \rho A\, \psi_i(x)\, \psi_j(x)\, dx \begin{bmatrix}\lambda_1 \\ \lambda_2 \\ \vdots \\ \lambda_n\end{bmatrix}$$

$$+ \begin{bmatrix}\lambda_1 & \lambda_2 & \cdots & \lambda_n\end{bmatrix} m_t\, \psi_i(L)\, \psi_j(L) \begin{bmatrix}\lambda_1 \\ \lambda_2 \\ \vdots \\ \lambda_n\end{bmatrix}.$$

Similarly, we can write the kinetic energy in matrix form as

$$T = \frac{1}{2}\, \vec{\lambda}^T [M]\, \vec{\lambda}, \tag{7}$$

where $[M]$ is the mass matrix of the system, defined by

$$M_{ij} = \int_0^L \rho A\, \psi_i(x)\, \psi_j(x)\, dx + m_t\, \psi_i(L)\, \psi_j(L). \tag{8}$$

2.1.3. Rayleigh's Quotient

The natural frequencies of the system can be determined using Rayleigh's quotient:

$$R = \omega^2 = \frac{V_{\max}}{T_{\max}} = \frac{N}{D}, \tag{9}$$

where N is the maximum strain energy, D is the maximum kinetic energy, and ω is the natural frequency. Rayleigh's quotient can be expressed as a function of the Ritz coefficients:

$$R = R(\lambda_1, \lambda_2, \ldots, \lambda_n). \tag{10}$$

To find the minimum of R, we take the partial derivative with respect to each Ritz coefficient and set it to zero:

$$\frac{\partial R}{\partial \lambda_i} = 0 \quad \text{for} \quad i = 1, 2, \ldots, n. \tag{11}$$

2.1.4. Eigenvalue Problem

Using the expressions for strain energy and kinetic energy,

$$N = \frac{1}{2}\,\vec{\lambda}^T[K]\,\vec{\lambda}, \quad D = \frac{1}{2}\,\vec{\lambda}^T[M]\,\vec{\lambda}, \tag{12}$$

and substituting into Rayleigh's quotient, we arrive at the generalized eigenvalue problem:

$$([K] - \Lambda^{(n)}[M])\,\vec{\lambda} = \vec{0}. \tag{13}$$

For a nontrivial solution $\vec{\lambda} \neq \vec{0}$, the determinant must vanish:

$$\left|[K] - \Lambda^{(n)}[M]\right| = 0. \tag{14}$$

The roots of this equation give the natural frequencies:

$$\omega_i = \sqrt{\Lambda_i^{(n)}}, \quad i = 1, 2, \ldots, n. \tag{15}$$

The corresponding eigenvectors $\vec{\lambda}^{(i)}$ follow from

$$([K] - \Lambda_i^{(n)}[M])\,\vec{\lambda}^{(i)} = \vec{0}. \tag{16}$$

Each mode shape is then given by

$$\mu^{(i)}(x) = \sum_{j=1}^{n} \lambda_j^{(i)}\,\psi_j(x). \tag{17}$$

2.1.5. Dynamic Response of the System

The total dynamic response of the system can be written as

$$Y(x,t) = \sum_{i=1}^{n} \mu^{(i)}(x)\,\eta_i(t), \tag{18}$$

where $\eta_i(t)$ are time-dependent generalized coordinates. The governing equation of motion is

$$EA\,\frac{\partial^2 Y(x,t)}{\partial x^2} + f(x,t) = \rho A\,\frac{\partial^2 Y(x,t)}{\partial t^2}. \tag{19}$$

Substituting the mode shape expansion yields

$$\sum_{i=1}^{n}\left[EA\,\frac{d^2\mu^{(i)}(x)}{dx^2}\right]\eta_i(t) + f(x,t) = \rho A \sum_{i=1}^{n} \mu^{(i)}(x)\,\frac{d^2\eta_i(t)}{dt^2}. \tag{20}$$

After further derivation and simplification, we obtain the modal form:

$$\frac{d^2\eta_i(t)}{dt^2} + \omega_i^2\,\eta_i(t) = Q_i(t), \tag{21}$$

where $Q_i(t) = \vec{\mu}^{(i)T}\,\vec{f}(t)$ is the generalized force corresponding to the i-th mode.

2.1.6. Solution Using the Laplace Transform
Applying the Laplace transform, we denote

$$L\{\eta_i(t)\} = \bar{\eta}_i(s), \quad L\{Q_i(t)\} = \bar{Q}_i(s). \tag{22}$$

The transform of the second derivative is

$$L\{\ddot{\eta}_i(t)\} = s^2\bar{\eta}_i(s) - s\,\eta_i(0) - \dot{\eta}_i(0). \tag{23}$$

Substituting into the modal equation, we have

$$\bar{\eta}_i(s) = \frac{\bar{Q}_i(s) + s\,\eta_i(0) + \dot{\eta}_i(0)}{\Delta}, \quad \Delta = s^2 + \omega_i^2. \tag{24}$$

Taking the inverse Laplace transform,

$$\eta_i(t) = \int_0^t Q_i(\tau)\,h(t-\tau)\,d\tau + g(t)\,\eta_i(0) + h(t)\,\dot{\eta}_i(0), \tag{25}$$

where

- $Q_i(\tau) = \int_0^L \mu^{(i)}(x)\,f(x,\tau)\,dx$,
- $h(t) = \frac{\sin(\omega_i t)}{\omega_i}$,
- $g(t) = \cos(\omega_i t)$,
- $\displaystyle\int_0^t Q_i(\tau)\,h(t-\tau)\,d\tau$ is the convolution integral (Duhamel's integral).

With the initial conditions $\eta_i(0) = 0$ and $\dot{\eta}_i(0) = 0$, the response simplifies to

$$\eta_i(t) = \int_0^t Q_i(\tau)\,h(t-\tau)\,d\tau. \tag{26}$$

Hence, the complete system response is

$$Y(x,t) = \sum_{i=1}^{n} \mu^{(i)}(x)\left[\int_0^t Q_i(\tau)\,h(t-\tau)\,d\tau\right]. \tag{27}$$

2.1.7. Trial Function

The trial functions $\psi_i(x)$ for the mode shape expansion are chosen as

$$\psi_i(x) = 1 - \cos\left(\frac{(2i-1)\,\pi\,x}{2L}\right), \quad i = 1, 2, \ldots, n, \tag{28}$$

which satisfy the boundary conditions of the beam and provide a suitable basis for approximating the mode shapes.

After this analytical derivation, the next step involves numerical simulations to examine the effects of parametric uncertainties (e.g., variations in material properties or geometry) on the structural dynamics of the beam–TMD system. These simulations are crucial for evaluating robustness and reliability under real-world operating conditions. In the following sections, we detail numerical examples, reliability assessments using sampling methods, and Monte Carlo simulations to estimate the probability of structural failure.

2.2. Numerical Study and Benchmarks

2.2.1. Numerical Example of Parameter Uncertainty on Structural Dynamics

The uncertainties in the base structure's properties are modeled as normal distributions, with the standard deviations presented in Table 1. Sample data for these properties are generated according to their respective distributions. Table 1 summarizes the statistical properties of the structural parameters considered in the longitudinal analysis of the seismic model. These parameters include the elastic modulus, density, and cross-sectional area, all of which are critical in determining the structure's dynamic behavior under seismic loading. Incorporating uncertainties in these parameters enables a more realistic assessment of structural performance.

Table 1: Nominal values and standard deviations of the structural parameters (longitudinal analysis).

Variables	**Mean**	**Standard Deviation**
Elastic Modulus (E)	2×10^{11}	3.6×10^{4}
Density (ρ)	7800	650
Cross-Sectional Area (A)	3.14×10^{-4}	3.14×10^{-5}

- **Elastic Modulus** (E): The mean value is 2×10^{11}, with a standard deviation of 3.6×10^4. This reflects the expected stiffness of the material and accounts for variations arising from material inconsistencies or imperfections. The relatively small standard deviation compared to the mean suggests that the material properties are fairly consistent, exhibiting limited variability.

- **Density** (ρ): The mean density is 7800, with a standard deviation of 650. Density influences the mass distribution within the structure, thereby affecting its natural frequency and dynamic response. The standard deviation constitutes approximately 8.3% of the mean value, indicating moderate variability potentially due to non-uniform material distribution or manufacturing processes.

- **Cross-Sectional Area** (A): The mean cross-sectional area is 3.14×10^{-4}, with a standard deviation of 3.14×10^{-5}. This parameter is essential for defining both stiffness and load-bearing capacity. The standard deviation accounts for 10% of the mean value, considering possible geometric inconsistencies during fabrication.

The seismic model possesses a nominal natural frequency of 25.224 rad/s and a damping ratio of 0.4. These dynamic characteristics are pivotal for understanding the system's response to stochastic inputs. The power spectral density (PSD) of the white noise excitation is set at $0.031\,\mathrm{m}^2/\mathrm{s}^3$, representing the input energy driving the structural vibrations.

A failure criterion is established as a displacement exceeding 0.028 m. By incorporating uncertainty in key structural parameters, this study aims to capture a broad spectrum of potential structural responses, offering a more comprehensive perspective on the likelihood of failure under stochastic loading conditions.

2.2.2. Feature Importance Using Random Forest Regression

To evaluate the influence of various features on the prediction of failure probability, we employ Random Forest Regression to compute feature importance scores. This approach facilitates the identification of the most impactful features in determining structural reliability, thereby enhancing our understanding of the factors contributing to the probability of failure.

Feature importance analysis provides critical insights into both the dataset and the predictive behavior of the model. By quantifying the significance of

each feature, we gain a deeper understanding of the key elements driving failure probability. This allows us to prioritize these influential features in future model developments. Additionally, the analysis aids in optimizing the model by highlighting less significant features that can be omitted to reduce computational complexity and improve efficiency without compromising predictive accuracy. Here, the Random Forest model is utilized to assess the importance of different mass units in a ten-degree-of-freedom structure equipped with a TMD. The results, based on a sample size of $N = 4000$, are presented in Table 2. .

Table 2: Feature Importance for Increased Standard Deviation of Elastic Modulus ($N = 4000$)

Feature	**Importance**
Density (ρ)	0.54881
Cross-Sectional Area (A)	0.35985
Elastic Modulus (E)	0.09133

To further investigate the role of the elastic modulus, the feature importance was calculated (Table 2). The updated importance scores are as follows: the importance of density (ρ) slightly decreased to 0.54881 but remained the most significant factor. The importance of cross-sectional area (A) reduced to 0.35985, still maintaining a notable effect. The elastic modulus (E) increased in importance to 0.09133, suggesting that its impact on the system dynamics becomes more significant with higher variability.

2.2.3. Reliability Analysis Using Latin Hypercube Sampling and Monte Carlo Simulation

To evaluate the reliability of the beam equipped with a Tuned Mass Damper (TMD) under dynamic loading, we employed Latin Hypercube Sampling (LHS) to generate sample realizations of the uncertain parameters. LHS is a stratified sampling method that ensures comprehensive coverage of each input distribution, leading to more accurate and robust estimates of failure probabilities. Subsequently, Monte Carlo simulation was utilized to estimate the failure probability of the beam system. This probabilistic approach involves running multiple iterations of the system model using the LHS-generated samples to observe the range of possible outcomes. The failure criterion was defined as a displacement exceeding 0.028 m, representing the

maximum allowable deformation to ensure structural integrity. Monte Carlo simulations determine the frequency with which the structural response surpasses this threshold. The combination of LHS and Monte Carlo simulation effectively captures the stochastic behavior of the system, enabling a comprehensive reliability assessment.

2.2.4. Performance Comparison

To assess the accuracy of failure prediction, various machine learning models were trained on the dataset generated from numerical simulations. The models evaluated include Random Forest, Gradient Boosting, Extreme Gradient Boosting (XGBoost), and Neural Networks. Each model exhibits unique strengths: Random Forest and Gradient Boosting are renowned for their ability to handle nonlinearity and robustness against overfitting, while Neural Networks excel in capturing complex relationships due to their layered architecture. The performance of each model was evaluated using the root mean square error (RMSE), mean absolute error (MAE), and relative error, as presented in Table 3.

Table 3: Performance Comparison of Machine Learning Models for Failure Probability Estimation

Model	**RMSE**	**MAE**	**Relative Error**
Random Forest	0.030384	0.021408	0.0916
Gradient Boosting	0.027676	0.020013	0.1070
XGBoost	0.030734	0.021780	0.0922
Neural Network	0.025835	0.018020	0.0117

The results summarized in Table 3 indicate that the Neural Network model outperformed the other models, achieving the lowest RMSE, MAE, and Relative Error. This suggests that the Neural Network is better suited to capture the complex nonlinear relationships inherent in the reliability analysis of the beam with a TMD. The Neural Network's superior performance can be attributed to its ability to learn intricate patterns and dependencies within the data, which are often difficult to capture with traditional ensemble methods like Random Forest and Gradient Boosting.

2.2.5. Scatter Plots of Predictions

Figure 3 provides a graphical comparison of the predicted versus true values for the Neural Network and XGBoost models. The scatter plots illustrate

the effectiveness of each model in predicting failure probability, with the red line representing the ideal scenario where predicted values perfectly match true values.

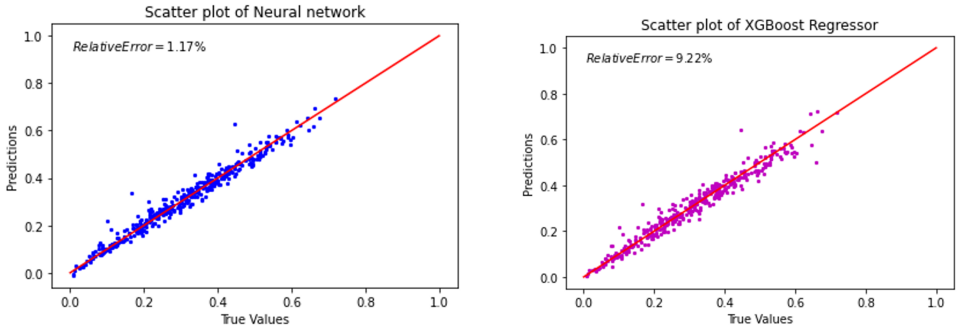

(a) Test vs. Predicted Values (Neural Network)

(b) Test vs. Predicted Values (XGBoost)

Figure 3: Performance Comparison of Different Machine Learning Models for Failure Probability Estimation. The Neural Network model consistently outperforms others in terms of lower error metrics, indicating its superiority in capturing the nonlinear relationships inherent in the data.

The scatter plot in Figure 3(a) shows that the Neural Network model's predictions are tightly clustered along the red line, indicating a high degree of accuracy with minimal relative error (1.17%). This suggests that the Neural Network model has successfully captured the complex underlying relationships between the input parameters and the structural response, resulting in highly accurate predictions. However, some outlier points can still be observed, which may indicate instances where the model struggled to accurately predict failure probability due to complex interactions or insufficient training data for specific regions of the input space.

In contrast, the XGBoost model's predictions, shown in Figure 3(b), display a greater spread around the red line, suggesting higher variability and a relative error of 9.22%. The presence of more numerous and larger outlier points implies that the model had difficulty fully capturing the intricate dependencies within the data, leading to less consistent predictions. This suggests that the XGBoost model may be less effective in handling the complex relationships between parameters in this context, and its predictive performance could be improved through further hyperparameter tuning or alternative feature engineering strategies. The visual comparison between

the models underscores the effectiveness of Neural Networks in scenarios involving highly nonlinear and interdependent variables, such as those present in structural dynamics.

2.2.6. Conclusion

The results demonstrate that machine learning techniques can effectively predict structural failures in dynamic systems, especially when dealing with complex and uncertain parameters. Among the models tested, the Neural Network exhibited significant advantages in terms of prediction accuracy, as evidenced by its lower RMSE, MAE, and Relative Error. This highlights the potential of Neural Networks in capturing the complex, nonlinear relationships present in the reliability analysis of mechanical systems with TMDs.

3. Transversal Vibration with a TMD

In the previous section, we examined the longitudinal vibrations of a beam equipped with a Tuned Mass Damper (TMD), focusing on axial displacements. Longitudinal vibrations, characterized by axial stretching and compression, primarily influence the beam's lengthwise behavior. However, in practical engineering applications, beams are often subjected to more complex forces, including transverse loads that induce vibrations perpendicular to the beam's axis.

Transversal vibrations involve both shear and bending deformations, making their analysis more intricate than that of longitudinal vibrations. Unlike longitudinal vibrations, which mainly affect the beam's length, transversal vibrations result in bending and significant lateral displacements. Transitioning from longitudinal to transversal vibration analysis is essential for a comprehensive understanding of the beam's dynamic behavior, especially under realistic loading conditions that encompass both bending and shear effects.

In this section, we investigate the dynamic response of beams subjected to transverse loading and assess the impact of bending and shear deformations on the structural behavior. This analysis is crucial for evaluating the effectiveness of TMDs in mitigating transverse vibrational effects in structural systems.

3.1. Transversal Shear and Bending Effects in Beam Dynamics

The transversal shear effect significantly influences a beam's dynamic response under loading. Unlike longitudinal vibrations, which involve axial

stretching or compression, transversal vibrations encompass complex shear and bending interactions that affect the structural integrity of the beam. Figure 4 illustrates the various deformation modes a beam can experience: (a) no deformation, (b) shear deformation only, (c) bending deformation only, and (d) total deformation.

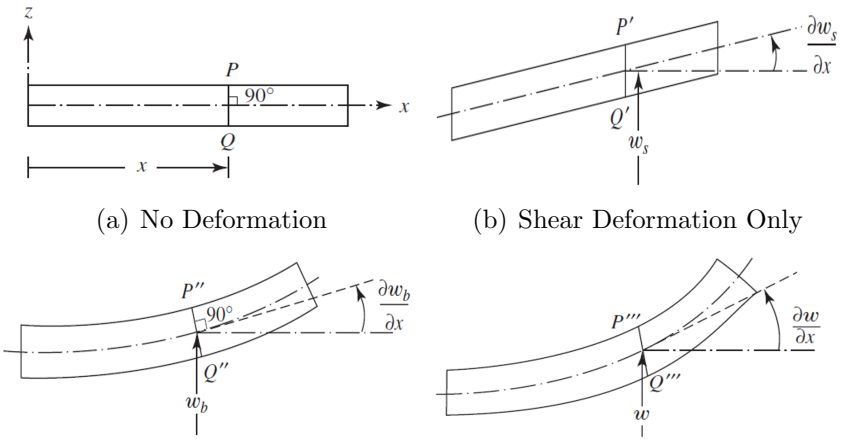

(a) No Deformation (b) Shear Deformation Only

(c) Bending Deformation Only (d) Total Deformation

Figure 4: Modes of Bending and Shear Deformations in a Beam. (a) No deformation, (b) shear deformation only, (c) bending deformation only, and (d) total deformation. These modes are essential for analyzing the effects of shear and bending on the beam's dynamic behavior.

The total transverse displacement of the beam's centerline is expressed as:

$$w = w_s + w_b \tag{29}$$

Consequently, the total slope of the beam is:

$$\frac{\partial w}{\partial x} = \frac{\partial w_s}{\partial x} + \frac{\partial w_b}{\partial x} \tag{30}$$

where:

- w_s is the shear deformation.
- w_b is the bending deformation.
- $\frac{\partial w_b}{\partial x}$ represents the rotation of the cross-section.

- $\frac{\partial w_s}{\partial x}$ denotes the shear angle.

The total slope accounts for both shear and bending deformations along the beam's length, directly affecting its vibrational characteristics.

To simplify the analysis, it is often assumed that the bending slope is negligible ($\frac{\partial w_b}{\partial x} = 0$), leading to:

$$\frac{\partial w}{\partial x} = \frac{\partial w_s}{\partial x} \tag{31}$$

Under this assumption, shear deformation predominates, allowing for a simplified equation of motion:

$$kGA\frac{\partial^2 w(x,t)}{\partial x^2} + f = \rho A\frac{\partial^2 w(x,t)}{\partial t^2} \tag{32}$$

where:

- k is the shear correction factor.
- G is the shear modulus.
- A is the cross-sectional area.
- ρ is the material density.
- f represents external forces.

In this equation, $kGA\frac{\partial^2 w}{\partial x^2}$ denotes the restoring force due to shear deformation, accounting for the beam's internal resistance influenced by G, A, and the shear correction factor k. The term $\rho A\frac{\partial^2 w}{\partial t^2}$ represents the inertial response, capturing the beam's dynamic reaction to time-varying loads. This formulation establishes the dynamic equilibrium of the beam under transverse loading, where internal shear forces balance external forces and inertial effects.

3.2. Analytical Analysis of Transversal Vibration

The horizontal displacement function for each mode is expressed as:

$$X(x,t) = \sum_{i=1}^{n} \lambda_i(t)\psi_i(x) \tag{33}$$

where $\lambda_i(t)$ is the time-dependent Ritz coefficient representing the contribution of each mode to the overall displacement, and $\psi_i(x)$ is the trial function describing the spatial variation of displacement.

The trial functions are chosen as:

$$\psi_i(x) = 1 - \cos\left(\frac{(2i-1)\pi x}{2L}\right), \quad i = 1, 2, \ldots, n \tag{34}$$

This selection ensures that the boundary conditions are satisfied and provides an accurate approximation of the beam's deformation shape. The cosine term captures the oscillatory nature of the deformation typical in vibration analysis, ensuring zero displacement at the fixed boundaries.

The boundary conditions for the beam are:

$$\begin{cases} X(0,t) = 0 & \text{(fixed end at } x = 0\text{)} \\ kGA\frac{\partial X(L,t)}{\partial x} = -k_t X(L,t) - c_t\frac{\partial X(L,t)}{\partial t} - m_t\frac{\partial^2 X(L,t)}{\partial t^2} & \text{(free end with TMD at } x = L\text{)} \end{cases} \tag{35}$$

The first condition ensures that the displacement is zero at the fixed end ($x = 0$). The second condition models the interaction between the beam and the TMD at the free end ($x = L$), incorporating the shear force in the beam, the restoring force from the spring (k_t), the damping force from the damper (c_t), and the inertial force from the mass (m_t) of the TMD.

3.2.1. Strain Energy of the System

The strain energy V of the system comprises contributions from both the beam and the spring element of the Tuned Mass Damper (TMD):

$$V = V_{\text{beam}} + V_{\text{spring}} \tag{36}$$

The strain energy stored in the beam is expressed as:

$$V_{\text{beam}} = \frac{1}{2}\int_0^L kGA\left(\frac{\partial X}{\partial x}\right)^2 dx \tag{37}$$

where G is the shear modulus, A is the cross-sectional area, and k is the shear correction factor. This term accounts for the energy due to shear deformation in the beam.

The strain energy in the TMD's spring is given by:

$$V_{\text{spring}} = \frac{1}{2}k_t X^2(L,t) \tag{38}$$

Here, k_t is the spring constant of the TMD, and $X(L,t)$ is the displacement at the free end of the beam where the TMD is attached.

Substituting the displacement function $X(x,t)$ into the strain energy expression, we obtain:

$$V = \frac{1}{2}\int_0^L kGA\left(\sum_{i=1}^{n}\lambda_i\psi_i'(x)\right)^2 dx + \frac{1}{2}k_t\left(\sum_{i=1}^{n}\lambda_i\psi_i(L)\right)^2 \tag{39}$$

Expanding this expression in matrix form yields:

$$V = \frac{1}{2}\begin{bmatrix}\lambda_1 & \lambda_2 & \cdots & \lambda_n\end{bmatrix}[K]\begin{bmatrix}\lambda_1\\ \lambda_2\\ \vdots\\ \lambda_n\end{bmatrix} \tag{40}$$

where $[K]$ is the stiffness matrix defined as:

$$K_{ij} = \int_0^L kGA\psi_i'(x)\psi_j'(x)\,dx + k_t\psi_i(L)\psi_j(L) \tag{41}$$

The stiffness matrix $[K]$ incorporates both the beam's material properties and the influence of the TMD, capturing the system's resistance to deformation.

3.2.2. Kinetic Energy of the System

The kinetic energy T of the system includes contributions from the beam and the mass attached to the TMD:

$$T = T_{\text{beam}} + T_{\text{mass}} \tag{42}$$

The kinetic energy of the beam is given by:

$$T_{\text{beam}} = \frac{1}{2}\int_0^L \rho A\left(\frac{\partial X}{\partial t}\right)^2 dx \tag{43}$$

where ρ is the material density and A is the cross-sectional area. This term represents the energy due to the beam's motion.

The kinetic energy of the TMD mass is expressed as:

$$T_{\text{mass}} = \frac{1}{2}m_t\left(\frac{\partial X}{\partial t}(L,t)\right)^2 \tag{44}$$

Here, m_t is the mass of the TMD, and $\frac{\partial X}{\partial t}(L,t)$ is the velocity of the mass at the free end of the beam.

Substituting the displacement function $X(x,t)$ into the kinetic energy expression, we obtain:

$$T = \frac{1}{2}\int_0^L \rho A \left(\sum_{i=1}^{n} \lambda_i \psi_i(x)\right)^2 dx + \frac{1}{2} m_t \left(\sum_{i=1}^{n} \lambda_i \psi_i(L)\right)^2 \tag{45}$$

Expanding this expression in matrix form yields:

$$T = \frac{1}{2}\begin{bmatrix}\lambda_1 & \lambda_2 & \cdots & \lambda_n\end{bmatrix}[M]\begin{bmatrix}\lambda_1 \\ \lambda_2 \\ \vdots \\ \lambda_n\end{bmatrix} \tag{46}$$

where $[M]$ is the mass matrix defined as:

$$M_{ij} = \int_0^L \rho A \psi_i(x)\psi_j(x)\,dx + m_t \psi_i(L)\psi_j(L) \tag{47}$$

The mass matrix $[M]$ represents the distribution of mass along the beam and the contribution from the TMD, playing a crucial role in determining the system's dynamic properties.

3.2.3. Rayleigh Quotient and Natural Frequencies

The Rayleigh quotient R is employed to estimate the natural frequencies of the system:

$$R = \omega^2 = \frac{N}{D} = \frac{V_{\max}}{T_{\max}} \tag{48}$$

where:

- N is the maximum strain energy,
- D is the maximum kinetic energy,
- ω is the natural frequency.

Expressed in terms of the Ritz coefficients, the Rayleigh quotient becomes:

$$R = R(\lambda_1, \lambda_2, \ldots, \lambda_n) \tag{49}$$

To determine the natural frequencies, we minimize R with respect to the Ritz coefficients:

$$\frac{\partial R}{\partial \lambda_i} = 0, \quad i = 1, 2, \ldots, n \tag{50}$$

This minimization condition identifies the optimal Ritz coefficients corresponding to the system's natural frequencies.

3.2.4. Eigenvalue Problem

Given the Rayleigh quotient:

$$R = \frac{N(\lambda_1, \lambda_2, \ldots, \lambda_n)}{D(\lambda_1, \lambda_2, \ldots, \lambda_n)} \tag{51}$$

taking the partial derivative and setting it to zero yields:

$$\frac{1}{D}\left(\frac{\partial N}{\partial \lambda_i} - \Lambda^{(n)} \frac{\partial D}{\partial \lambda_i}\right) = 0 \tag{52}$$

Rearranging terms leads to the matrix form of the eigenvalue problem:

$$\left([K] - \Lambda^{(n)}[M]\right) \vec{\lambda} = \vec{0} \tag{53}$$

For a nontrivial solution, the determinant must satisfy:

$$\left|[K] - \Lambda^{(n)}[M]\right| = 0 \tag{54}$$

Solving this equation provides the natural frequencies $\omega_i = \sqrt{\Lambda_i^{(n)}}$ for $i = 1, 2, \ldots, n$. The eigenvalues $\Lambda_i^{(n)}$ represent the squared natural frequencies, which are fundamental to understanding the dynamic behavior of the beam-TMD system.

3.2.5. Mode Shapes and Dynamic Response

Once the eigenvalues $\Lambda_i^{(n)}$ are determined, the corresponding mode shapes $\vec{\lambda}^{(i)}$ are obtained by solving:

$$\left([K] - \Lambda_i^{(n)}[M]\right) \vec{\lambda}^{(i)} = \vec{0} \tag{55}$$

Each mode shape represents a distinct spatial deformation pattern of the beam associated with a specific natural frequency. These mode shapes provide insight into how the structure dynamically deforms under vibration.

The dynamic response of the system is expressed as:

$$Y(x,t) = \sum_{i=1}^{n} X^{(i)}(x)\eta_i(t) \tag{56}$$

where $\eta_i(t)$ are the generalized coordinates describing the time evolution of each mode. These coordinates govern the amplitude variation of each mode over time.

The equation of motion for each mode is given by:

$$\ddot{\eta}_i(t) + \omega_i^2 \eta_i(t) = Q_i(t) \tag{57}$$

where $Q_i(t)$ is the generalized force corresponding to the ith mode, defined as:

$$Q_i(t) = \int_0^L X^{(i)}(x) f(x,t)\, dx \tag{58}$$

This second-order differential equation describes how each mode responds to external forcing.

3.2.6. Solution of the Equation of Motion

The solution to the equation of motion incorporates convolution integrals, known as Duhamel's integral, to account for the effects of external forces over time. The dynamic response is thus:

$$Y(x,t) = \sum_{i=1}^{n} X^{(i)}(x) \left[\int_0^t Q_i(\tau) h_i(t-\tau)\, d\tau \right] \tag{59}$$

where the impulse response function $h_i(t)$ for each mode is:

$$h_i(t) = \frac{\sin(\omega_i t)}{\omega_i} \tag{60}$$

This function characterizes the system's reaction to an instantaneous force, and the convolution integral represents the cumulative effect of the applied force over time. Thus, it fully describes the dynamic response of the beam-TMD system.

3.3. Numerical Study and Benchmarks

3.3.1. Numerical Example of Parameter Uncertainty on Structural Dynamics

The uncertainties in the base structure properties are modeled as normal distributions with standard deviations presented in Table 4. By incorporating these uncertainties into the structural parameters, the analysis captures a broader range of potential structural responses, providing a more comprehensive assessment of the structure's reliability under seismic loading conditions. Understanding the influence of these parameters facilitates better-informed decisions in structural design and optimization, ultimately enhancing safety and performance.

Table 4: Nominal Values and Uncertainties of Structural Parameters (Transversal Vibration)

Variable	Mean	Standard Deviation
Shear Modulus (G)	52.5 GPa	5 GPa
Density (ρ)	7800 kg/m^3	650 kg/m^3
Cross-Sectional Area (A)	3.14×10^{-2} m^2	3.14×10^{-3} m^2

3.3.2. Feature Importance Using Random Forest Regression

To evaluate the impact of different features on predicting failure probability, we employ Random Forest Regression to derive feature importance scores.

Table 5: Feature Importance for Failure Prediction ($N = 20000$)

Feature	**Importance**
Cross-Sectional Area (A)	0.34138
Density (ρ)	0.33700
Shear Modulus (G)	0.32162

When the sample size increased to $N = 20000$, as shown in Table 5, the feature importance scores became more balanced. The cross-sectional area (A) had an importance score of 0.34138, density (ρ) was at 0.33700, and shear modulus (G) at 0.32162. This indicates that a larger sample size reduces the disparity among feature importance scores, offering a more comprehensive view of the relative contributions of each parameter.

Overall, the analysis demonstrates that while the cross-sectional area (A) remains the most significant factor across different sample sizes, the roles of density (ρ) and shear modulus (G) are also crucial, particularly as more data is incorporated.

3.3.3. Performance Comparison of Machine Learning Models for Failure Probability

To further assess the reliability of the transverse vibration beam equipped with a Tuned Mass Damper (TMD) under dynamic loading, several machine learning models were trained on datasets representing transversal vibrations. The performance of these models is summarized in Table and 6.

Table 6: Performance of Machine Learning Models for Failure Probability Prediction ($N = 20000$)

Model	**RMSE**	**MAE**	**Relative Error**
Random Forest	0.011775	0.009263	1.86%
Gradient Boosting	0.008923	0.008923	1.79%
XGBoost	0.011541	0.009100	1.82%
Neural Network	0.012610	0.010012	0.20%

Table 6 compares the performance for a larger dataset size of $N = 20000$. All models demonstrated improved performance with the increased dataset size, attributable to a better representation of the underlying probabilistic distribution of the input parameters. The Gradient Boosting model continued to lead with the lowest RMSE (0.008923) and MAE (0.008923), alongside a Relative Error of 1.79%. Both XGBoost and Random Forest benefited from the larger dataset, showing reductions in RMSE and MAE, though the improvements were less significant compared to Gradient Boosting.

The Neural Network model, despite achieving the lowest Relative Error (0.20%), displayed higher RMSE and MAE than Gradient Boosting, indicating potential overfitting issues. The model may have learned the training data excessively well, thereby reducing its generalization capacity when applied to new data. In contrast, the Random Forest and XGBoost models maintained balanced performance with moderate RMSE and MAE, demonstrating robustness without significant overfitting.

3.3.4. Distribution of Predicted Failure Probability

Figure 5 presents the distribution of predicted failure probabilities for a sample size of $N = 20000$. The histogram indicates that the probability of failure approximates a normal distribution, offering insights into the reliability and behavior of the beam structure.

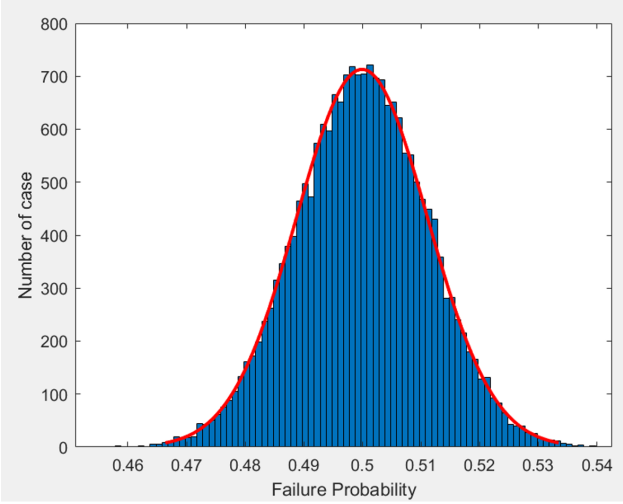

Figure 5: Distribution of Predicted Failure Probability for Beam Structure ($N = 20000$). The probability distribution closely follows a normal distribution, highlighting consistent and predictable reliability behavior.

The distribution plot in Figure 5 shows that the predicted failure probabilities are centered around a mean value of approximately 0.5, with most cases falling within a relatively narrow range. This suggests consistent and predictable failure behavior under the given loading conditions. The red curve, representing a fitted normal distribution, closely aligns with the histogram of predicted values, indicating that the variability in failure probability is symmetrically distributed around the mean.

Overall, the analysis demonstrates that Gradient Boosting consistently yields the best balance of error metrics, particularly for large datasets. Neural Networks show potential, especially in minimizing Relative Error, but require careful tuning to avoid overfitting. Random Forest and XGBoost provide good robustness and reliability across different dataset sizes, making them strong candidates when computational efficiency and generalizability are priorities.

3.3.5. Scatter Plots of Predictions

Figure 6 presents a graphical comparison of predicted versus true values for the Neural Network and Random Forest models across different dataset sizes.

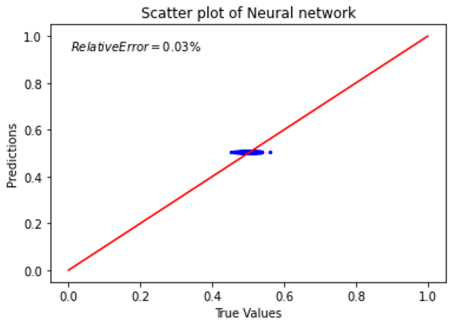

(a) Neural Network Predictions ($N = 5000$)

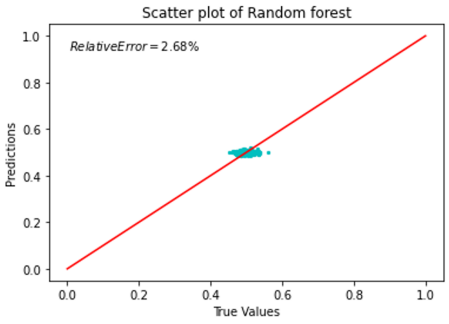

(b) Random Forest Predictions ($N = 5000$)

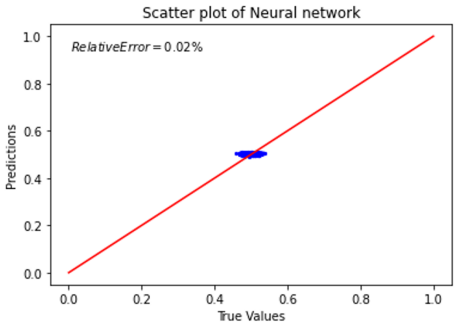

(c) Neural Network Predictions ($N = 20000$)

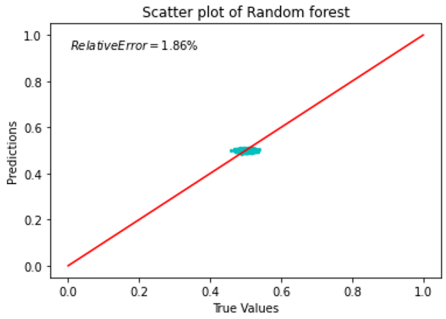

(d) Random Forest Predictions ($N = 20000$)

Figure 6: Comparison of Machine Learning Model Predictions for Failure Probability Estimation. The Neural Network model consistently outperforms other models, particularly with larger datasets, as evidenced by lower prediction errors and better alignment with actual values.

The scatter plots in Figure 6 provide insights into the performance of the machine learning models in predicting failure probability. Subfigures 6(a) and 6(c) illustrate the Neural Network model's predictions for datasets of sizes $N = 5000$ and $N = 20000$, respectively. The predicted values are plotted against the true values, with a reference line representing perfect agreement. For the Neural Network model, the data points closely cluster around the reference line, particularly for the larger dataset ($N = 20000$), indicating a

high degree of accuracy. The relative error of 0.02% for $N = 20000$ further confirms the model's improved performance with increased data.

Subfigures 6(b) and 6(d) display the Random Forest model's performance for the same dataset sizes. While the Random Forest model also demonstrated improved accuracy with larger datasets, as evidenced by the reduction in relative error from 2.68% to 1.86%, the scatter plots indicate slightly greater dispersion around the reference line compared to the Neural Network model. This suggests that while Random Forest provides reliable predictions, it may not capture the underlying patterns as precisely as the Neural Network, especially for complex relationships between input features and failure probabilities.

Overall, the comparison underscores the strengths and limitations of each approach. The Neural Network model consistently outperforms the Random Forest in prediction accuracy, particularly with larger datasets. However, the Random Forest remains a viable option, offering a balance between interpretability and robustness.

3.3.6. Trade-offs Between Machine Learning Models

The comparison of machine learning models highlights critical trade-offs between prediction accuracy, model complexity, and computational cost.

The Gradient Boosting model offers high accuracy and low error metrics but is relatively more complex and computationally intensive compared to Random Forest and XGBoost. This higher computational demand may be a limitation in situations with constrained resources or where rapid model updates are required. Additionally, Gradient Boosting is less interpretable, making it harder to understand the specific contributions of each feature to the final predictions—a drawback in applications where model transparency is critical.

Random Forest provides a good trade-off between performance and interpretability. Its ensemble-based structure allows for robust predictions while remaining relatively straightforward to understand. However, Random Forest may not perform as well as Gradient Boosting in capturing complex non-linear interactions, leading to slightly higher error metrics, especially for smaller datasets.

Similar to Gradient Boosting, XGBoost offers high accuracy but often requires careful hyperparameter tuning to avoid overfitting. It can be computationally demanding, particularly for large datasets, but due to its parallel processing capabilities, it is typically more efficient than traditional Gradi-

ent Boosting. This makes XGBoost a preferred choice when computational efficiency is needed without significantly sacrificing accuracy.

Neural Networks have the potential for extremely low error metrics, especially with larger datasets, as observed in the scatter plot analysis. However, their susceptibility to overfitting and the significant computational resources required for training make them challenging to use effectively. They also lack the interpretability of tree-based models, which can be a major drawback in applications where understanding model behavior is essential. Despite these challenges, Neural Networks are well-suited for capturing complex, non-linear relationships that other models might struggle with.

4. Conclusion

In this section, we successfully conduct continuous modeling of dynamic systems, emphasizing the increased complexity and accuracy required to represent real-world structures effectively. The Rayleigh-Ritz method proved effective in approximating the behavior of continuous systems by converting partial differential equations into a more tractable form.

Using Latin Hypercube Sampling and Monte Carlo simulation, we thoroughly assessed the reliability of beam structures with TMDs, accounting for the stochastic nature of loading and material properties. Additionally, the application of machine learning models, such as Random Forests and Neural Networks, facilitated the prediction of failure probabilities and offered valuable insights into the factors affecting structural reliability.

5. Experimental reliability analysis of the two-storey steel frame structure stochastic conditions

5.1. Experimental Rig

A suite of measurement and excitation components was employed to ensure accurate and reliable data acquisition throughout the tests. The core instrumentation included a 4-channel m+p VibPilot data acquisition system, a Brüel & Kjær (B&K) Type 4809 shaker, a B&K Type 2706 power amplifier, a NEXUS conditioning amplifier, one force transducer, and one accelerometer.

The experimental setup, depicted in Fig. 7, was meticulously designed to represent a two-degree-of-freedom (2-DOF) structural system. In this configuration, each degree of freedom corresponds to the lateral displacement

of a storey within the rigid frame structure. Specifically, the 2-DOF system examined herein consists of a two-storey rigid frame constructed from steel members, ensuring sufficient stiffness and well-defined mass distribution. The structure was mounted onto a heavy steel table to provide a fixed boundary condition at its base.

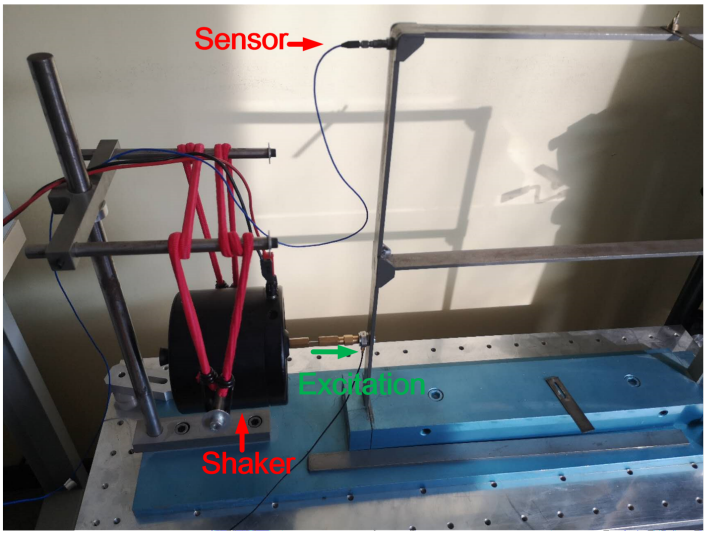

Figure 7: Experimental setup.

A mechanical shaker, positioned on the left side of the structure, served as the dynamic excitation source. This shaker was connected to the structure through a force transducer, ensuring accurate measurement of the input force. By converting electrical signals into controlled mechanical vibrations, the shaker imposed horizontal dynamic loads that mimic various excitation conditions, such as broadband noise or harmonic sweeps. The operating frequency range of the shaker and the input signal type (random, harmonic, or sweep) were adjustable, allowing for a comprehensive investigation of the structure's frequency response and mode shapes.

To measure the resulting horizontal accelerations, an accelerometer with a sensitivity of approximately $10\,\mathrm{mV}/g$ was attached to the top storey. The chosen accelerometer sensitivity and mounting technique ensured stable, repeatable measurements with minimal signal noise. Together with the force transducer mounted at the base-level interface, these instruments enabled the direct capture of both input and output signals, forming the foundation for dynamic characterization and model validation.

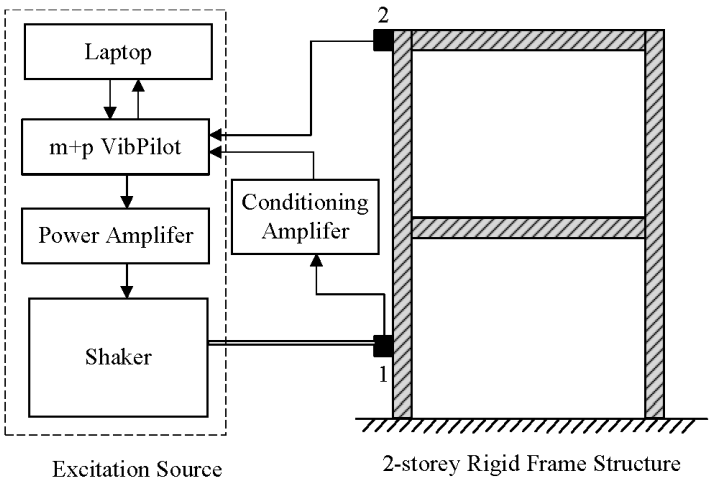

Figure 8: Schematic diagram of the experiment (1. Force transducer, 2. Accelerometer).

Figure 8 presents a schematic diagram of the experimental arrangement. The setup is divided into three key subsystems:

1. **Excitation Source**: The mechanical shaker and force transducer responsible for applying dynamic loads.
2. **2-Storey Rigid Frame Structure**: The steel frame representing the structural system under investigation.
3. **Data Acquisition and Processing**: Instruments and systems for capturing and analyzing input and output signals.

The experiment was conducted along the x axis, ensuring that the test structure effectively behaved as a planar (2D) system. This simplification allowed for a focused analysis of lateral dynamics, including building sway, resonances, and energy dissipation mechanisms.

5.1.1. Signal Generation Approach

To investigate the influence of higher-order statistical parameters on measurement and analysis outcomes, a comprehensive set of synthetic random signals was generated. These signals systematically varied in terms of Kurtosis, Root Mean Square (RMS) amplitude, Skewness, and Crest Factor. A total of 3,600 distinct signals were created using MATLAB, each serving as an input stimulus for subsequent analyses conducted in the m+p Analyzer environment.

All signals were band-limited random waveforms spanning a frequency range of 20 Hz to 2 kHz. This bandwidth was selected to reflect typical ranges encountered in mechanical vibration testing, ensuring relevance to modal analysis and structural health monitoring applications. An initial Gaussian random noise signal was generated as a baseline, featuring a flat spectral content within the specified bandwidth and an RMS amplitude normalized to 1.0 arbitrary units.

This systematic approach to signal generation ensured that the experimental analyses could effectively isolate and evaluate the impact of varying statistical parameters on the structural dynamics of the beam system. By controlling and varying these parameters, the study aimed to enhance the understanding of how different signal characteristics influence the reliability and accuracy of dynamic measurements and analyses.

5.1.2. Structural Response Measurements

A force transducer, mounted between the shaker and the structure, measured the horizontal excitation force. Simultaneously, an accelerometer installed at the top level of the structure recorded the structural response. The specific mounting positions were chosen to capture critical dynamic behavior: the force transducer near the base provided a direct input measurement, while the accelerometer at the top recorded responses most influenced by higher modes and flexible behavior. This instrumentation strategy facilitated a comprehensive assessment of the structure's dynamic properties, including stiffness, damping, and mass distribution.

5.1.3. Data Acquisition and Analysis Procedures

The m+p VibPilot unit served as both a signal generator and a data acquisition device. It produced the excitation signals while simultaneously recording the force and acceleration data. By collecting 6.4 seconds of raw time-domain data for each test configuration, a sufficiently large dataset was obtained for reliable spectral estimation, filtering, and subsequent modal analysis. Both online monitoring and offline post-processing were performed using the m+p Analyzer software, allowing for immediate validation of test signals and, later, detailed frequency-domain and time-domain analysis.

5.2. Summary of the Experimental Procedure

In summary, the experimental procedure involved configuring the input signal parameters on the laptop, generating excitation signals through the m+p

VibPilot, amplifying these signals via the power amplifier, and delivering controlled dynamic loads to the structure using the shaker. The force and acceleration responses were measured by the force transducer and accelerometer, respectively, and recorded by the m+p VibPilot. This allowed for a comprehensive dynamic characterization of the structure, both in its baseline state and with added Tuned Mass Dampers (TMDs). The collected data provided the foundation for subsequent analyses, including the evaluation of surrogate models and their potential for improving the dynamic performance of multi-storey structures.

5.3. Measurement of Test Data

5.3.1. Excitation Force Measurement

The input force delivered to the test structure originates from the shaker's moving armature and reaction mass. By measuring the acceleration of these moving components and knowing their mass, the applied force can be computed. In practice, a force transducer is placed in series between the shaker and the structure to directly capture the input force. This transducer converts mechanical force into a proportional electrical signal, which is then amplified and conditioned before being recorded by the m+p VibPilot data acquisition system.

5.3.2. Response Acceleration Measurement

Similarly, the horizontal acceleration response of the top floor of the structure is measured using an ICP accelerometer. The raw acceleration signal is recorded in volts and then converted into engineering units of acceleration (in g) using the sensor's known sensitivity (e.g., $10\,\mathrm{mV}/g$). The m+p VibPilot system, configured through the m+p Analyzer software, automatically applies the appropriate scaling to ensure accurate acceleration readings.

Figures 9(a) and 9(b) illustrate typical time histories of the excitation force and the resulting acceleration for one of the test runs. The time-domain signals highlight how the structure responds over the 6.4-second measurement interval and form the basis for subsequent analyses, such as frequency-domain decomposition, modal parameter identification, and comparison with numerical models.

5.4. Linkages Between Experimental and Theoretical Studies

Traditional theoretical models of structural dynamics, such as lumped-mass and finite element models, focus on parameters like mass, stiffness, and damp-

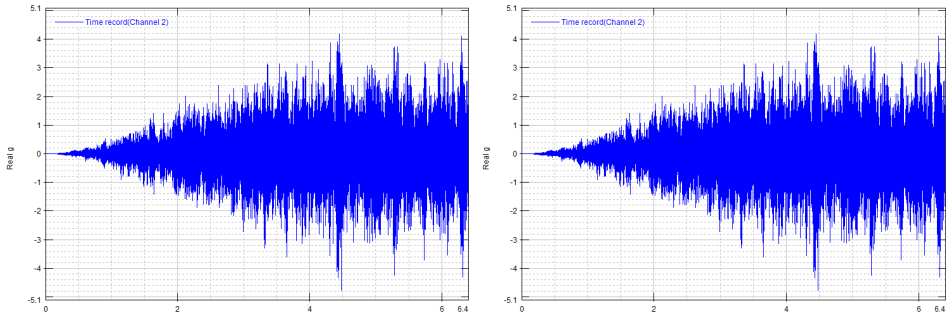

(a) Force-Time History (b) Acceleration-Time History

Figure 9: Typical Time Histories of Excitation Force and Structural Acceleration. (a) Force-Time History illustrating the input excitation over time. (b) Acceleration-Time History showing the corresponding structural response.

ing to characterize mechanical behavior. However, the complexity of real-world vibration signals and the presence of potential nonlinearities or subtle damage mechanisms mean that relying solely on these traditional parameters may not fully capture the system's behavior.

In this research, a data-driven shift is introduced by employing machine learning (ML) models that utilize statistical features extracted from raw vibration signals. Instead of using physical parameters (mass, stiffness, damping) as direct inputs to predictive models, time-domain statistical features—such as kurtosis, root mean square (RMS), skewness, and crest factor—are computed from the measured acceleration signals.

In essence, the transition from traditional mechanical parameters to statistical features marks a shift toward a more data-driven paradigm. While physical parameters remain crucial for conceptual understanding and design, statistical features serve as informative inputs to ML models, capturing complex, real-world phenomena. This integrated approach—combining physical insights with data-driven feature extraction—provides a more holistic and flexible framework for analyzing and interpreting vibration data, ultimately improving the accuracy of fault detection, structural health monitoring, and predictive maintenance strategies.

5.5. Inputs and Outputs of the Machine Learning Models

In this study, four time-domain features of the vibration signals were chosen as input variables for the machine learning (ML) models: kurtosis, Root Mean Square (RMS) amplitude, skewness, and crest factor. These statistical

parameters were extracted from the measured acceleration response signals of the structural system. They were selected based on their relevance to characterizing vibration signals, their capacity to capture both amplitude-related behavior and waveform shape characteristics, and prior knowledge that such features can reveal nonlinearities, impulsive events, or other complex dynamics not always apparent through conventional modal parameters alone.

5.5.1. Dataset Construction

A total of 3600 datasets were generated. Each dataset comprised four time-domain statistical features as inputs and one output representing the corresponding failure probability. The data collection process involved subjecting the structure to 100 random excitation realizations under controlled laboratory conditions. For each realization, the structural displacement response was recorded, and a deterministic displacement threshold was set to define the failure limit state. If the measured displacement exceeded this threshold at any point in time, a "failure" was recorded for that particular realization.

The probability of failure for each dataset was computed as the fraction of realizations (out of 100) that exhibited a first-passage event beyond the prescribed threshold. By repeating this procedure under various test conditions, 36 distinct input-output datasets were assembled, each reflecting a unique combination of excitation conditions and structural responses.

5.5.2. Output Variable

The output variable was the failure probability, calculated as the proportion of excitation realizations that resulted in displacement exceeding the predefined threshold. This probabilistic measure serves as a direct indicator of the structural reliability under varying dynamic loading conditions.

5.6. Model Performance Comparison

We compared the performance of four machine learning (ML) models—Random Forest, Gradient Boosting, XGBoost, and Neural Network—using a dataset of $N = 36$ observations, each derived from the mean response of a series of vibration tests. The models were evaluated based on their predictive accuracy for the probability of failure (PoF) using standard metrics: Root Mean Square Error (RMSE), Mean Absolute Error (MAE), and Relative Error (%).

Table 7 summarizes the performance metrics for the four models. The Random Forest model achieves the lowest RMSE and MAE, indicating a

more accurate and robust prediction of failure probabilities given the limited dataset size. Gradient Boosting, XGBoost, and Neural Network models exhibit slightly higher RMSE and MAE values, suggesting they are comparatively less effective at capturing the underlying relationships with the given number of samples and features. Nevertheless, all models demonstrate reasonable performance, and their ranking could shift with different sample sizes or feature sets.

Table 7: Comparison of Model Performance Metrics (N=36)

Model	**RMSE**	**MAE**	**Relative Error (%)**
Random Forest	0.036	0.032	0.18
Gradient Boosting	0.047	0.035	0.20
XGBoost	0.053	0.043	0.23
Neural Network	0.040	0.032	0.23

The Random Forest model outperforms the other models with the lowest RMSE and MAE, reflecting its superior ability to accurately predict failure probabilities within the constraints of a small dataset. Gradient Boosting and XGBoost also perform well but are slightly less effective than Random Forest. The Neural Network model, while showing competitive MAE and Relative Error, has a higher RMSE, indicating greater variability in its predictions.

5.6.1. Scatter Plots of Predicted vs. Actual Failure Probabilities

Figure 10 compares the predicted failure probabilities from four machine learning models—Random Forest (RF), Gradient Boosting (GB), eXtreme Gradient Boosting (XGB), and Neural Network (NN)—against the actual values. Each subplot represents a specific model, plotting predicted values on the vertical axis against true values on the horizontal axis. Ideally, perfect predictions would align all data points along the 45-degree diagonal line.

Among the models assessed, the Random Forest demonstrated the lowest RMSE, MAE, and relative error, indicating superior prediction accuracy and reliability for this dataset and feature set. In contrast, the GB, XGB, and NN models exhibited greater dispersion in their scatter plots (Figure 10), suggesting that these models did not fully leverage the available training data or feature set. This may be due to the sample size limiting their ability to capture complex nonlinear relationships.

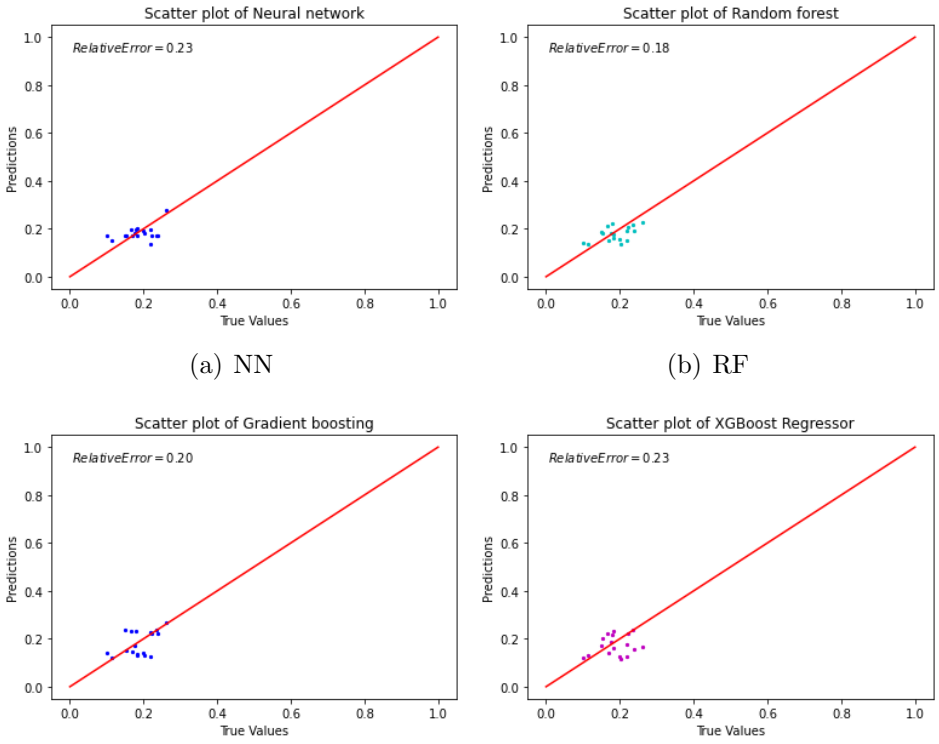

(a) NN (b) RF

(c) GB (d) XGB

Figure 10: Predicted vs. Actual Failure Probabilities for Different ML Models

5.6.2. Relative Errors of Four ML Models

Figure 11 compares the relative errors of four machine learning (ML) models across four key time-domain features: kurtosis, skewness, RMS, and crest factor. Each subplot focuses on one feature, with the feature's measured value on the horizontal axis and the relative error (expressed as a percentage) on the vertical axis.

Kurtosis (Fig. 11(a)). In the kurtosis subplot, the RF, GB, and XGB models exhibit consistently low relative errors across the entire range of kurtosis values. This indicates that these ensemble-based models effectively capture the "peakedness" or tail heaviness of the distribution. The NN model occasionally achieves lower errors but shows intermittent spikes at certain kurtosis values, suggesting less consistent performance. Overall, RF, GB, and XGB provide more reliable predictions for kurtosis, whereas the NN may require

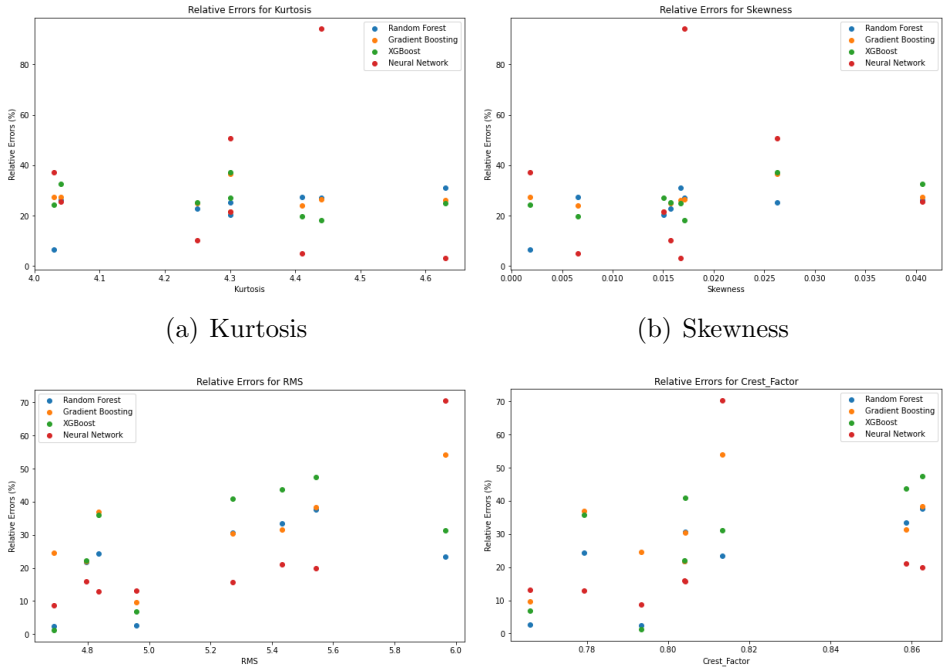

(a) Kurtosis (b) Skewness

(c) RMS (d) Crest Factor

Figure 11: Relative Error Distributions for Different ML Models Across Key Time-Domain Features

additional tuning or more data to enhance stability.

Skewness (Fig. 11(b)). For skewness, which measures the asymmetry of the distribution, all four models maintain low and consistent relative errors, especially within the mid-range of skewness values. This suggests that capturing asymmetry in the signal distribution is relatively straightforward for these ML models. Although the NN exhibits minor fluctuations, its performance is largely comparable to the other models.

RMS (Fig. 11(c)). Examining RMS (a measure of signal energy), the RF and XGB models achieve lower and more consistent relative errors across a broad range of RMS values. In contrast, the NN demonstrates increasing errors at higher RMS values, potentially reflecting difficulties in accurately capturing energy-related variations under certain conditions. The GB model performs moderately, offering steady performance without the extremes seen in the NN. These results suggest that ensemble methods like RF and XGB

are more robust and reliable for energy-related signal characteristics.

Crest Factor (Fig. 11(d)). The crest factor subplot reveals that the RF and XGB models produce comparatively lower and more consistent errors, even as crest factor values increase. Conversely, the NN and, to a lesser extent, the GB model occasionally exhibit higher errors at certain crest factor levels. Since the crest factor highlights transient peaks or spikes in the signal, these findings imply that ensemble methods better capture and model transient behaviors compared to the current NN configuration, which might benefit from further tuning or additional training data.

Overall, the ensemble-based ML models (RF, GB, and XGB) generally outperform the NN in terms of relative error consistency and reliability across different time-domain features.

6. Conclusion

This study bridges the gap between high-fidelity theoretical models of continuous systems and practical experimental investigations of multi-storey frame structures to deliver a robust framework for structural reliability analysis. In the beam-like continuous systems, the Rayleigh-Ritz method proved effective for approximating both longitudinal and transverse vibrations, while Tuned Mass Dampers provided a viable solution for mitigating resonance and reducing dynamic responses. Monte Carlo simulation and Latin Hypercube Sampling facilitated a thorough reliability assessment, highlighting key uncertainties in loading and system parameters. Experimental validation on a two-storey steel frame showed that data-driven approaches could detect and model complex vibrational behaviors not fully captured by traditional mechanical parameters alone. Time-domain statistical features (kurtosis, RMS, skewness, and crest factor) served as strong predictors of structural failure probabilities when fed into machine learning algorithms. Among these, Random Forest and certain ensemble methods offered robust performance across varied input conditions, emphasizing their potential for widespread adoption in structural health monitoring applications. This work unifies theoretical, numerical, and experimental perspectives to demonstrate the value of a multi-pronged strategy for dynamic analysis and reliability evaluation. The findings affirm that incorporating ML-based surrogate models can deepen our understanding of intricate system behaviors, while carefully designed experiments anchor numerical predictions in observable phenomena. Collectively,

these insights pave the way toward more resilient structural designs, efficient maintenance protocols, and safer built environments.

References

[1] R. E. Barlow, F. Proschan, Mathematical Theory of Reliability, Society for Industrial and Applied Mathematics, 1996. doi:10.1137/1.9781611971194.
URL https://epubs.siam.org/doi/abs/10.1137/1.9781611971194

[2] S. Menard, Applied logistic regression analysis, Sage, 2002.

[3] J. E. Hurtado, Structural Reliability: Statistical Learning Perspectives, Vol. 17, Springer Berlin Heidelberg, 2004. doi:10.1007/978-3-540-40987-8.

[4] H. M. D. Kabir, A. Khosravi, M. A. Hosen, S. Nahavandi, Neural network-based uncertainty quantification: A survey of methodologies and applications, IEEE Access 6 (2018) 36218–36234. doi:10.1109/ACCESS.2018.2836917.

[5] L. Q. Minh, P. L. T. Duong, M. Lee, Global sensitivity analysis and uncertainty quantification of crude distillation unit using surrogate model based on gaussian process regression, Industrial Engineering Chemistry Research 57 (2018) 5035–5044. doi:10.1021/acs.iecr.7b05173.
URL https://doi.org/10.1021/acs.iecr.7b05173

[6] Y. Peng, P. Sun, Reliability-based design optimization of tuned mass-damper-inerter for mitigating structural vibration, Journal of Sound and Vibration 572 (2024) 118166.

[7] H. B. de Salles, L. F. F. Miguel, M. S. Lenzi, R. H. Lopez, Reduced-order model for rbdo of multiple tmds on eccentric l-shaped buildings subjected to seismic excitations, Mechanical Systems and Signal Processing 206 (2024) 110906.

[8] L. F. F. Miguel, S. Elias, A. T. Beck, Reliability-based optimization of supported pendulum tmds' nonlinear track shape using padé approximants, Engineering Structures 306 (2024) 117861.

[9] W. Ma, Y. Yang, J. Yu, G. Yang, Improving processing stability of thin-walled casing workpieces by sucker-mounted tmd: Optimization, design, and implementation, Mechanical Systems and Signal Processing 216 (2024) 111512.

[10] S. H. Crandall, W. D. Mark, Random vibration in mechanical systems, Academic Press, 2014.

[11] J. Roberts, First-passage probabilities for randomly excited systems: diffusion methods, Probabilistic Engineering Mechanics 1 (2) (1986) 66–81.

[12] Q. X. Lieu, K. T. Nguyen, K. D. Dang, S. Lee, J. Kang, J. Lee, An adaptive surrogate model to structural reliability analysis using deep neural network, Expert Systems with Applications 189 (2022) 116104.

[13] X.-Q. Li, L.-K. Song, G.-C. Bai, Recent advances in reliability analysis of aeroengine rotor system: a review, International Journal of Structural Integrity 13 (1) (2022) 1–29.

[14] Y. Peng, T. Zhou, J. Li, Surrogate modeling immersed probability density evolution method for structural reliability analysis in high dimensions, Mechanical Systems and Signal Processing 152 (2021) 107366.

[15] Z.-A. Li, X.-W. Dong, C.-Y. Zhu, C.-H. Chen, H. Zhang, Vectorial surrogate modeling method based on moving kriging model for system reliability analysis, Computer Methods in Applied Mechanics and Engineering 432 (2024) 117409.

[16] H. Fan, C. Wang, S. Li, Novel method for reliability optimization design based on rough set theory and hybrid surrogate model, Computer Methods in Applied Mechanics and Engineering 429 (2024) 117170.

[17] W. You, Reliability assessment of tmd-based control structures: A statistical learning perspective, Ph.D. thesis, Université de Lyon (2020).

[18] I. Venanzi, Robust optimal design of tuned mass dampers for tall buildings with uncertain parameters, Structural and Multidisciplinary Optimization 51 (2015) 239–250.

[19] S. Marelli, B. Sudret, An active-learning algorithm that combines sparse polynomial chaos expansions and bootstrap for structural reliability analysis, Structural Safety 75 (2018) 67–74. doi:https://doi.org/10.1016/j.strusafe.2018.06.003.
URL https://www.sciencedirect.com/science/article/pii/S0167473017302977

[20] R. Schöbi, B. Sudret, S. Marelli, Rare event estimation using polynomial-chaos kriging, ASCE-ASME Journal of Risk and Uncertainty in Engineering Systems, Part A: Civil Engineering 3 (6 2017). doi:10.1061/AJRUA6.0000870.

[21] A.-H. Tian, C.-B. Fu, Y.-C. Li, H.-T. Yau, Intelligent ball bearing fault diagnosis using fractional lorenz chaos extension detection, Sensors 18 (2018). doi:10.3390/s18093069.
URL https://www.mdpi.com/1424-8220/18/9/3069